Journal of Inorganic and Organometallic Polymers and Materials
https://doi.org/10.1007/s10904-025-03628-4

RESEARCH

First Principles Calculation on the Physical Attributes of Cubic Perovskites $SbXO_3$ (X = Al and Ga) for Renewable Energy Devices Application

Jisha Annie Abraham[1] · Arti Saxena[2] · Jaidev Kumbhakar[3] · Anshuman Srivastava[4] · Ahmed Ahmed Ibrahim[5] · Mohammed El-Meligy[6,7] · Mumtaz Manzoor[8] · Ramesh Sharma[9]

Received: 5 October 2024 / Accepted: 20 January 2025

Abstract
In this research article, we present a density functional theory (DFT) oriented analysis to examine the optoelectronic and thermoelectric properties, along with the mechanical stability, of two proposed oxide perovskites, $SbAlO_3$ and $SbGaO_3$, based on the full potential linear augmented plane wave (FP-LAPW). The evaluated formation energy E_F and tolerance factor (τ_F) show that considered perovskite-oxides were thermodynamically optimum with cubic cell. Generalized gradient approximation (PBE-GGA) along modified Beck Johnson potential (TB-mBJ) potential confirms direct bandgaps (E_g) of 2.074 and 2.059 eV for $SbXO_3$ (X=Al, Ga), respectively. The optical characteristics were investigated in the energy range of 0–10 eV. Optimal energy loss suggesting plasma resonance is at 9 eV and above 10 eV, maximum reflectivity at 52.12% and 56.96% at 6.25 eV and 7.50 eV for SbGaO3 and $SbAlO_3$ respectively. Furthermore, thermoelectric features are determined using semiclassical Boltzmann theory with constant relaxation time approximation. Calculated figure of merit (zT) values for $SbXO_3$ (X=Al, Ga) are 0.40 and 0.68 at 1200 K, respectively. Thermal parameters are crucial in establishing a material's thermal endurance over a broad spectrum of temperatures. We anticipate that the estimated characteristics of $SbAlO_3$ and $SbGaO_3$ compounds will pave the way for novel applications in optoelectronics and thermoelectric devices.

Keywords DFT · Direct bandgap · Absorption coefficient · Seebeck coefficient · Lattice thermal conductivity

1 Introduction

The search for environmentally acceptable and sustainable energy sources includes the utilization of thermoelectric materials, which convert waste heat into electricity. Increased energy use necessitates the development of new energy sources to meet the world's energy constraint. For this goal, several kinds of materials and processes are examined to determine the most cost-effective, affordable, and simple ways to generate energy. Because of their excellent thermal stability and low lattice thermal conductivity, oxide-based systems were effective in switching waste heat

✉ Ramesh Sharma
sharmadft@gmail.com

[1] Department of Physics, National Defence Academy, Pune 411023, India

[2] Present address: Department of Electronics & Communication, Pranveer Singh Institute of Technology, Kanpur, UP, India

[3] Department of Mechanical Engineering, Nirwan University, Jaipur, India

[4] Department of Mechanical Engineering, Shambhunath Institute of Engineering and Technology, Prayagraj, India

[5] Department of Physics and Astronomy, College of Science, King Saud University, P.O. Box 2455, 11451 Riyadh, Saudi Arabia

[6] Jadara University Research Center, Jadara University, PO Box 733, Irbid, Jordan

[7] Applied Science Research Center, Applied Science Private University, Amman, Jordan

[8] Institute of Physics, Slovak Academy of Sciences, 84511 Bratislava, Slovakia

[9] Department of Applied Science, Feroze Gandhi Institute of Engineering and Technology, Raebareli, India

Published online: 31 January 2025

into useable electrical energy [1–3]. Perovskites are used in a variety of devices, including non-linear optics, optoelectronics, electro-optics, photovoltaic solar cell systems, as well as numerous other thermoelectric applications at 300 K [4]. As a result, these semiconducting systems are being extensively researched around the world for their viability for usage in a wide range of applications. Antimony chalcogenides as well as Bismuth-based solid solutions were observed to be high-efficiency devices that can be employed in many thermoelectric applications [5]. To be used in such applications, potential systems ought to possess low heat conductivity, a high Seebeck coefficient (S), and high electrical conductivity (σ/τ). Among the chalcogenide family, the semiconductor Bi_2Se_3 has been researched for thermoelectric purposes [6]. Now a days, Scientists are intrigued in identifying potential ternary semiconductors for photoelectric and thermoelectric technology because of their excellent thermoelectric properties, low effective mass, direct band gap, as well as higher optical absorption coefficient [7, 8]. The two distinct characteristics of perovskite materials—ferroelectric and piezoelectric—make them useful for applications such as ferroelectric random-access memory, sensors, transformers, and capacitors [9, 10]. According to [11], Pb-based piezoelectric materials can be readily modified by substituting non-magnetic elements for M in $BiMO_3$ (M=Al, Ga, In, and Sc). Synthesis of these compounds has made considerable use of high-pressure and temperature techniques [12]. Sheng Ju and colleagues (2019) examined the harmonics in $BiXO_3$ (X=In, Al) using fundamental principles and discovered their use in non-linear optoelectronics [13]. The structural, electrical, and optical characteristics of cubic perovskite ($BaCeO_3$) have been extensively researched recently by a number of researchers [14, 15]. This development may add a new dimension and physical properties to these compounds and create new avenues for their application in optoelectronics and optomagnonics [16, 17]. The optical characteristics of $BiMO_3$ (M=Al, Ga, and In) have been computationally investigated and published in literature [18]. Ferroelectricity was anticipated theoretically in $BiAlO_3$ and experimentally in $BiGaO_3$, where it was found not to exist. Thus, the analysis of cubic $BiAlO_3$ and $BiGaO_3$ from first principles provides comprehension into the formation of ferroelectricity in $BiMO_3$ systems and helps us understand how structural and electrical properties differ from one another. In the literature, these are clearly stated [19]. DFT approaches were employed to investigate the physical properties of unit and hexagonal cell [20, 21]. $BiAlO_3$ with (R3c:161) at 300 K [22] has proven that a strong covalent bonding is present between Al 3p, Bi 6p, and O-2p orbitals in $BiAlO_3$. We have uncovered soft mode among high-symmetry sites X and Γ that drives the rhombohedral-cubic phase transition, as well as the structure of the zone-center model's rhombohedral phase of frequencies. To produce $BiAlO_3$, Acharya et al. 2020 [23] used a pulse laser deposition approach [9, 24], which resulted in the breakdown of Bi_2O_3 and $Bi_{24}Al_2O_{40}$ and no perovskite phase. They proposed that to evaluate the potential of ferroelectric systems found in high-throughput databases, more synthesizability descriptors are required. In their quest for novel and unusual ferroelectric materials, Zhao et. al. published phase transition having high symmetry breaking in AA'3B4O12 type A-site ordered perovskites in 2021 [24]. Relied on considerations made employing the full potential linearized augmented plane wave (FP-LAPW) approach, the researchers reported the physical characteristics of $BiAlO_3$, $BiGaO_3$, and $BiInO_3$ systems [25]. $BiMO_3$'s refractive index, dielectric function, absorption coefficient, and energy loss have all been investigated.

Nazir et al. explored optoelectronic and thermoelectric response of alkali based half-Heusler semiconductors AMgN (A=Rb, Cs) for sustainable energy by DFT [26]. High Spin Polarization and half-metallic ferromagnetism in novel Half–Heusler FeCrX (X=S, Se and Te) alloys were derived by Abrar and his colleagues using first-principles calculations for energy applications. Their results reveal that FeCrTe is best material Due to the higher value of Seebeck coefficient, power factor, figure of merit, and electrical conductivity, FeCrTe is the best material for transport applications [27]. Hossain et al. computed the Hydrothermal Synthesis, Phase Analysis, and Magneto-Electronic Characterizations of Lead-Free Ferroelectric BM^{2+}(Zn, Ca, Mg) T–BFO System [28]. Uddin et al. calculated the Optoelectronic and Photovoltaic Properties of Lead-Free $Cs_2AgBiBr_6$ Double Perovskite Solar Cells Using DFT [29]. Uddin et al. finds the Performance improvement and optimization of $Cs_2TiI_2Br_4$ perovskite solar cells with diverse charge transport materials via numerical analysis [30]. Gherriche et al. computed detailed ab initio investigation of the structural, elastic, electronic and optical properties of a new layered perovskite-type oxyfluoride: $CsSrNb_2O_6$ [31]. Bouhemadou performed to study in details the structural, elastic, electronic, chemical bonding and optical properties of Cu-based ternary oxides ACuO (A=Li, Na, K and Rb) [32]. Qaisi et al. finds the Structural, elastic, mechanical and thermodynamic properties of Terbium oxide [33]. Khenata et al. computed the structural and electronic properties of GeC, SnC and GeSn by DFT [34].

In similar line of research, in order to enhance the physical behaviours and characteristics of $SbXO_3$ (X=Al and Ga), this work attempts to explore all of these qualities (optical and electrical). Our research is also crucial to enhancing the applications of these substances in various optoelectronic devices. We will also demonstrate through this study that $SbXO_3$ materials (where X is equal to Al or Ga) have optical

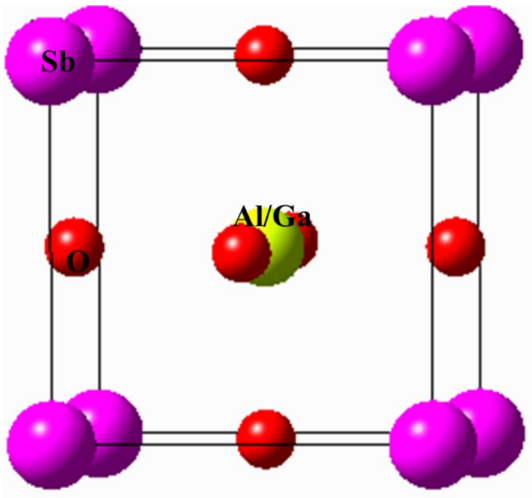

Fig. 1 Crystal structures of cubic Perovskite $SbXO_3$ (X=Al, Ga)

characteristics that make them a viable option for optoelectronic as well as thermoelectric applications. We designed the paper so that the computation details are provided in Sect. 2. The computed results are presented and discussed in Sect. 3. We conclude the paper with a brief conclusion in the final section.

2 Computational and Details

The crystal structure of $SbXO_3$ (X=Al, Ga) is represented in Fig. 1. Several DFT calculation techniques, such as LDA and GGA, are available under the first-principles method and can be performed with the use of multiple codes [25, 35]. We employed PBE-GGA, TB-mBJ, and [26–38] integrated with the WIEN2k code[25, 39]. The interstitial sites and the non-over-lapping atomic spheres are integrated into the unit cell without any approximations. The FP-LAPW method's potential grows as follows (inside the sphere)

$$V(r) = \sum_{lm} V_{lm}(r) Y_{lm}(\widehat{r}) \tag{1}$$

(beyond the sphere)

$$V(r) = \sum_{k} V_k e^{ikr} \tag{2}$$

where $Y_{lm}(\widehat{r})$ represents the product of spherical harmonics and linearly combined radial function. Atomic muffin-tin (MT) radii of Sb, Al, Ga and O are 2.00 a.u., 2.00 a.u., and 1.50 a.u., in that order. The K_{max} value can be ascertained by multiplying the muffin-tin radii by the Maximum wave vector, which equals 7. The cut-off energy for the energy gap is set to − 6.0 Ry. While optoelectronic properties are identified using a denser mesh with 10,000 k-points, the tetrahedron approach uses 35 k-points to integrate over the Brillouin zone. To determine the thermoelectric retort of examined oxides, we employ the BoltzTraP code [40], which is based on semi classical Boltzmann transport theory. The BoltzTrap parameters (σ/τ, κ/τ, and S) are mounted by the constant relaxation time (τ). The real values could be approximated executing a suitable relaxation time, which includes the T plus carrier concentration.

3 Results and Discussion

3.1 Structural Properties

The structure of the $SbXO_3$ (X=Al, Ga) crystal is depicted in Fig. 1. After the volume optimization, the studied compounds have lattice constant a=3.7661 Å and 3.8847 Å, respectively and X atoms are positioned at (0.5, 0.5, 0.5), Sb at (0, 0, 0) and O at (0.5 0 0). Computed values of ground state properties of $SbXO_3$ are displayed in Table 1. As illustrated in Fig. 2, the experimental obtained data of the lattice constants for cubic perovskite $SbXO_3$ was utilized to minimize the energy using the Birch–Murnaghan equation, that developed from the literature [41].

$$E(V) = E_0 + \frac{B}{B\prime(B\prime - 1)}\left[V\left(\frac{V_0}{V}\right)^{B\prime} - V_0\right] + \frac{B}{B\prime}(V - V_0) \tag{3}$$

where B-bulk modulus, $B\prime$- its pressure derivative, V_0-equilibrium volume.

To increase reliability, $SbXO_3$ (X=Al, Ga) perovskite oxides should be studied for structural and thermodynamic stability. The structural stability is ensured by the tolerance factor [39].

$$t = 0.707\frac{\langle r_{Sb-}r_X\rangle}{\langle r_{X-}r_O\rangle} \tag{4}$$

Table 1 Calculated lattice parameter *a* (A°), bulk modulus *B*, its derivative B_P, the minimum total energy E_{tot}, enthalpy of formation E_f and tolerance factor of $SbXO_3$(X=Al, Ga) by PBE-GGA

XC	a (Å)	B (GPa)	B_P	E_{tot} (Ry)	E_f (KJ/mol)	t_c
$SbAlO_3$	3.7661	190.8493	4.5038	− 13,904.700511	− 921.35	0.84
$SbGaO_3$	3.8847	193.2096	5.5764	− 17,307.034543	− 564.48	0.81

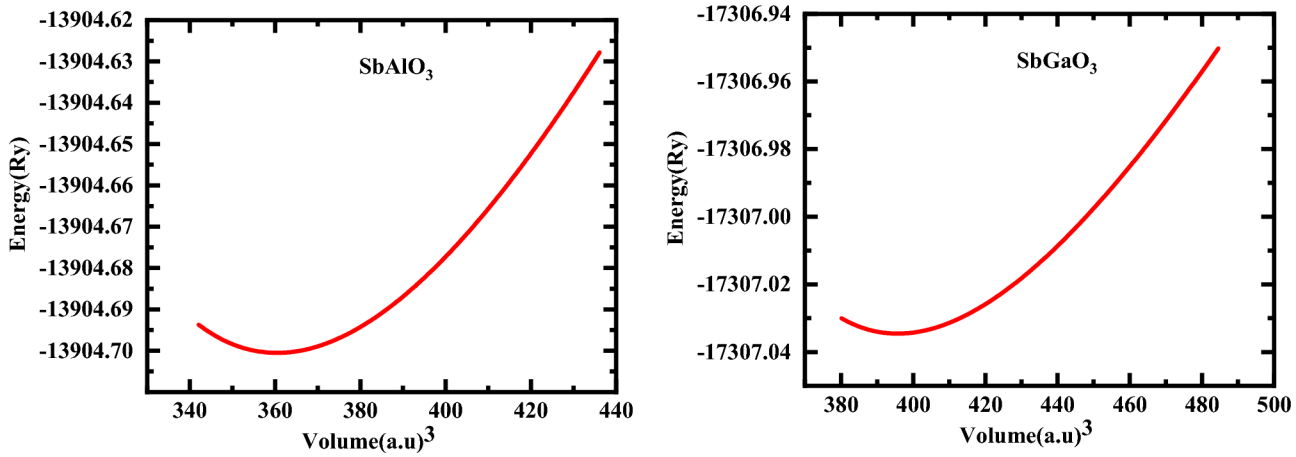

Fig. 2 Total energy (Ry) versus total volume ($a.u^3$) for cubic perovskites $SbXO_3$ (X=Al, Ga) calculated for PBE-GGA methods

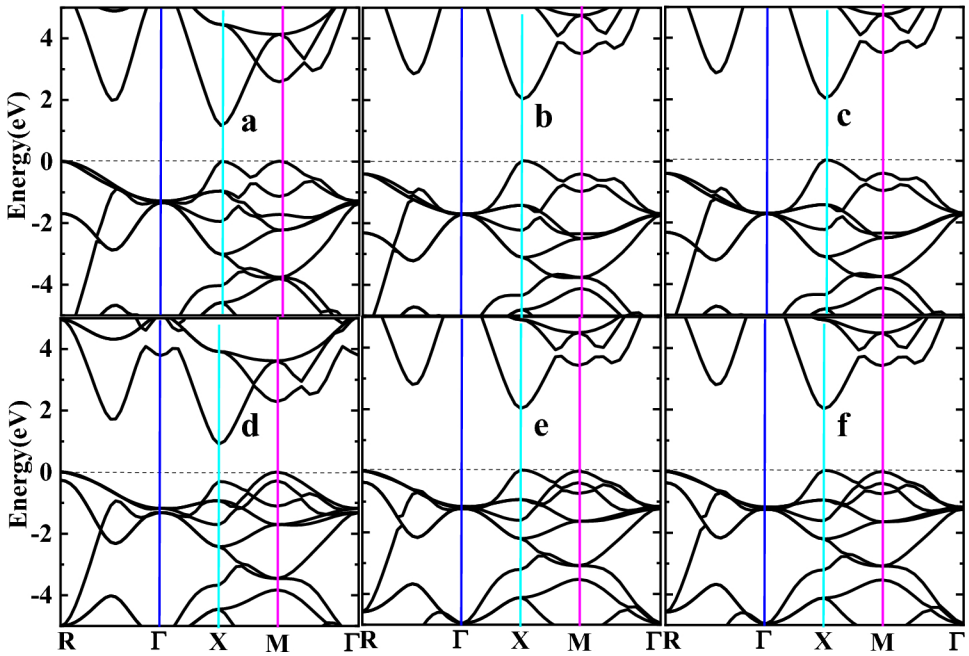

Fig. 3 Band structure **a** PBE-GGA **b** mBJ **c** mBJ+SOC for of $SbAlO_3$, (d) PBE-GGA (e) mBJ (f) mBJ+SOC calculations for and $SbGaO_3$

For cubic phase, the standard range of tolerance factor is 0.8—1.0. Our computed tolerance factor estimates lie in the specified range, demonstrating that the examined oxides can certainly develop in the cubic phase (see Table 1).

Furthermore, thermodynamic solidity is also essential for device consistency. Using below equation, the formation energies of the perovskites were also calculated to assess their chemical stability. The energy of Sb, X, and O (X=Al, Ga) atoms is represented by E(Sb), E(O), and E (Al, Ga) for the corresponding atoms, while the total energy of the $SbXO_3$ (X=Al and Ga) unit cell is represented by Etot ($SbXO_3$).

$$\Delta E_f = \frac{E_{tot}\,(\mathrm{SbXO3}) - E\,(Sb) - E\,(X) - 3E(O)}{5} \tag{5}$$

As per calculation, obtained value of formation energy is found to be -921.35 kJ/mol for $SbAlO_3$ and -564.48 kJ/mol for $SbGaO_3$. The variation of total energy with volume of $SbXO_3$ (X=Al, Ga) crystal considering the potential PBE-GGA is shown in Fig. 2a, b. It is observed in the calculation that best fitting is observed with PBE-GGA, where the minimum energy is obtained for $SbGaO_3$ (– 17,307.034543 Ry) rather than $SbAlO_3$ (– 13,904.700511Ry), which displays that $SbGaO_3$ is more stable than $SbAlO_3$, as represented in Table 1.

3.2 Electronic Properties

The computed electronic band structure of $SbXO_3$ compounds employing PBE-GGA, mBJ-GGA and mBJ+SOC functionals along high symmetry directions

Table 2 Calculated energy bandgap (in eV) by different potentials PBE, mBJ and mBJ+SOC

Properties	PBE	mBJ	mBJ+SOC	References
$SbAlO_3$	1.235	2.074	1.99	[4, 51, 52, 53]
$SbGaO_3$	0.959	2.059	1.96	

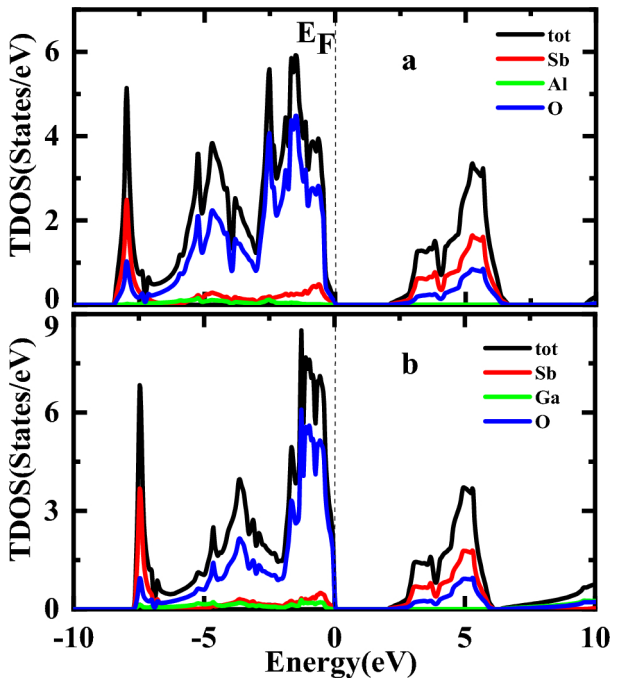

Fig. 4 Total density of states (TDOS) of cubic perovskites **a** $SbAlO_3$ **b** $SbGaO_3$

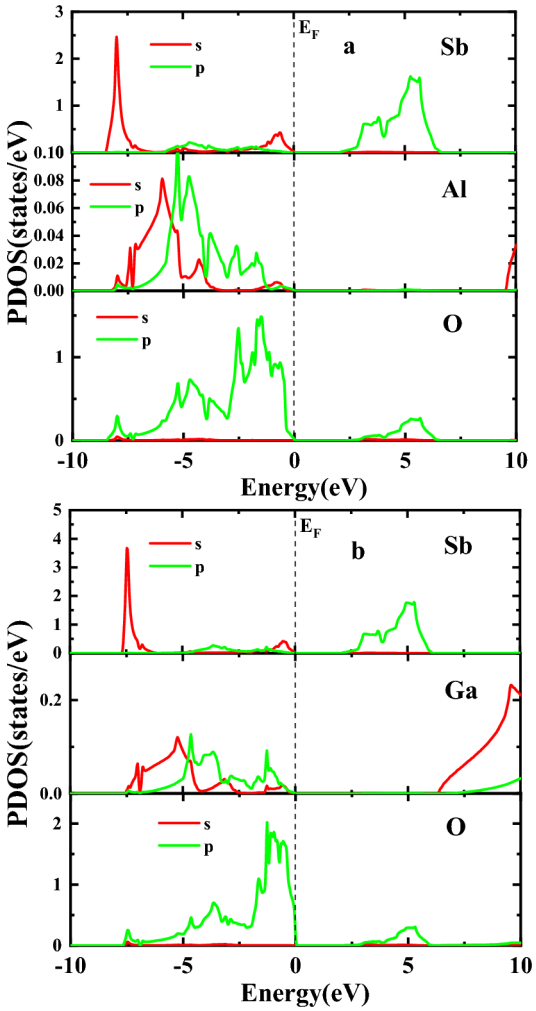

Fig. 5 The partial density (PDOS) of states (TDOS) of cubic perovskites **a** $SbAlO_3$ **b** $SbGaO_3$

$R-\Gamma-X-M-\Gamma$ are shown in Fig. 3a–f. The electronic band structures are found to have direct band gap at Γ point for SbAlO3 with all the three approximations, whereas for SbGaO3, using PBE-GGA, an indirect band gap of 0.959 eV along $X-M$. The band gap values of $SbAlO_3$ and $SbGaO_3$ using PBE-GGA, mBJ-GGA, and mBJ-GGA+SOC are illustrated in Table 2. Comparatively large value of energy band gap is measured in mBJ potential scheme. Subsequently, we employed mBJ+SOC potentials to explore the $SbXO_3$ (X=Al (1.99) and Ga (1.96)) bandgap values. The band gap is identified as an indirect band gap. The top of the valence band (VB) and bottom of the conduction band (CB) are made up of O-2p as well as Sb-5p orbitals, correspondingly. The obtained results of electronic states of nonmagnetic $SbXO_3$ (X=Al, Ga) are similar to the electronic profiles of recently reported BaPaO3, BaUO3 [42, 43], BaNpO3 [16] perovskites.

In order to validate the results of the energy band structure analysis, the Total as well as Partial Density of States (TDOS & PDOS) were calculated and presented in Figs. 4, 5. Fermi level is set at 0 eV. From about -10 eV to 10 eV, the energy graphs are displayed. Positive energy is associated with conduction band (CB) states, while negative energy is associated with valence band (VB) states. In both conduction and valence bands that resemble the band structure, TDOS displays sum of the various states. Figure 4(a–d) elaborates on the PDOS for the compounds under study, which depict the orbital contribution to the electron conduction process. Hybridization of the Sb-4d and O-5p orbitals along with slight contribution from Al/Ga 's' & 'p' states is responsible for the creation of the valence band in $SbAlO_3$. In the meantime, the hybridization of O-5p as well as Sb-4d states has occupied the conduction band. The formation of the valence band in $SbGaO_3$ is attributed to the hybridization of Ga-5p and O-5p electrons, with a nominal contribution from Sb-6 s. Nonetheless, hybridization of Ga-4d and O-4d states occupies the conduction band.

Figure 6 displays the charge density distributions in two dimensions for the (110) plane. To fully understand the electronic structure of the system under study, charge density maps are a useful supplementary tool. Any material's ionic character can be linked to the transfer of charge between its

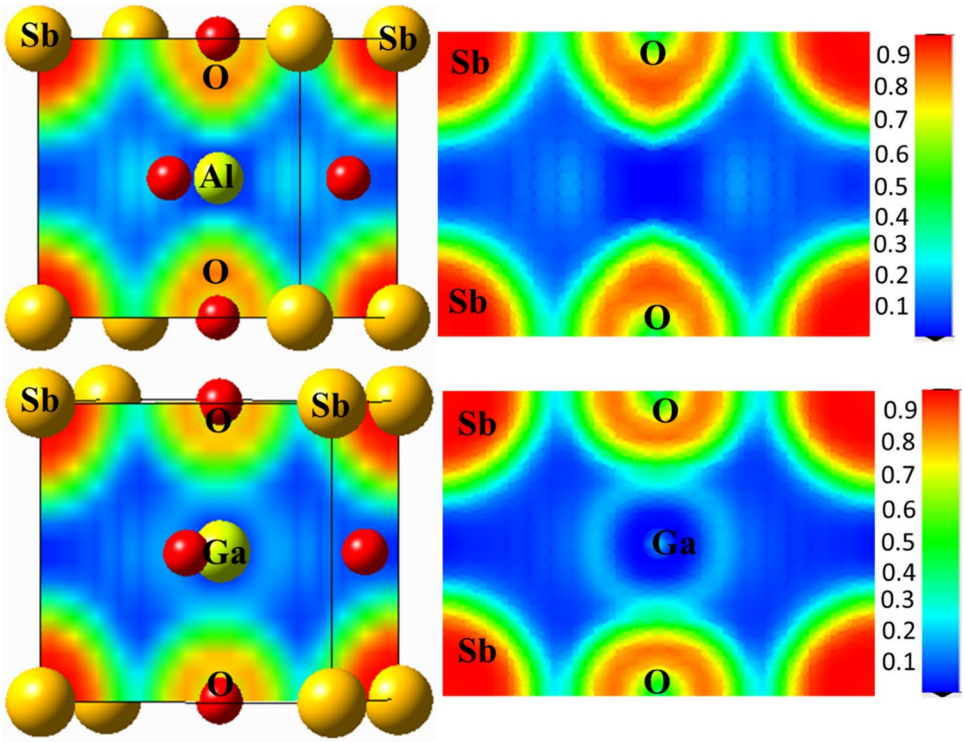

Fig. 6 Electron localization function along 110 plane **a** $SbAlO_3$ **b** $SbGaO_3$

cation and anion, whereas covalent character is related to the sharing of charge between the cation and anion. Al/Ga and O have a covalent nature, but Sb and O appear to have feeble ionic bond based on the charge density contours. From Fig. 6, it is clear that s and p orbitals of Al and Ga mix together, and a new orbital is formed at the same energy, thus there is a strong hybridization in valence band.

3.3 Optical Properties

So as to determine the significance of the investigated materials for solar cell applications, the optical properties were thoroughly investigated. Examined was the optical performance of the valence to conduction band transition study. The relative placements of materials and light serve to highlight the optical qualities. The inter as well as intra-band transitions govern the strength of light emission and absorption in optoelectronic devices. With the aid of its dielectric behaviour, which is defined by its dielectric function, any material's optical properties can be determined with the relation: $(\omega)=\varepsilon_1(\omega)+i\varepsilon_2(\omega)$. Its imaginary part $\varepsilon_2(\omega)$ describes the characteristics of absorption [34, 35] can be expressed as follows:

$$\varepsilon_2(\omega) = \frac{4\pi e^2}{m^2\omega^2}\sum_{i,j}\int_k \langle i|M|j\rangle^2 f_i(1-f_i)\times\delta(E_{j,k}-E_{i,k}-\omega)\,d^3k \tag{6}$$

where M as a dipole matrix, i and j are initial and final states, respectively. Here f_i—Fermi distribution function &—$E_i$the electron's energy in the i[th] state with crystal wave vector k, respectively. The dielectric function's real portion, $\varepsilon_1(\omega)$, can be found using the Kramers–Kronig relation [43, 44]:

$$\varepsilon_1(\omega) = 1 + \frac{2}{\pi}\int_0^{\infty}\frac{\omega\prime\varepsilon_2(\omega\prime)\,d\omega\prime}{\omega'^2-\omega^2} \tag{7}$$

Once the real and imaginary portions' values are known, we can compute the optical characteristics by using the corresponding relations: Refractive index provides information on the interface as well as transmission of illumination through material in a relationship,

$$n(\omega) = \left\{\frac{\varepsilon_1(\omega)}{2} + \frac{\sqrt{\varepsilon_1(\omega)^2+\varepsilon_2(\omega)^2}}{2}\right\}^{1/2} \tag{8}$$

The extinction coefficient provides a substance's absorption characteristics at a particular wavelength in proportion to,

$$k(\omega) = \left\{\frac{\varepsilon_1(\omega)}{2} - \frac{\sqrt{\varepsilon_1(\omega)^2+\varepsilon_2(\omega)^2}}{2}\right\}^{1/2} \tag{9}$$

Luminescence provides information about a material's ability to absorb and re-emit light with a relationship of

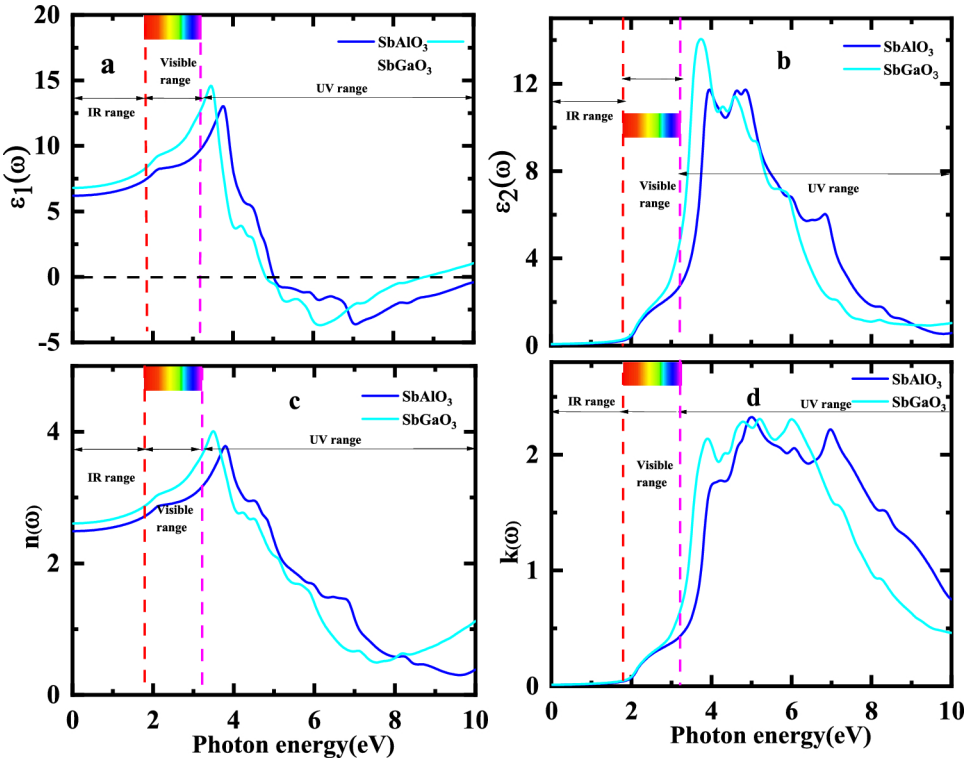

Fig. 7 **a** Real part $\varepsilon_1(\omega)$, **b** Imaginary part $\varepsilon_2(\omega)$, **c** Refractive index $n(\omega)$, and (d) extinction coefficient $k(\omega)$ for $SbXO_3$ (X=Al, Ga)

$$L(\omega) = Im\left(-\frac{1}{\varepsilon(\omega)}\right) \tag{10}$$

A system's overall energy drop is determined by energy loss, which has the following relation:

$$\alpha(\omega) = \frac{4\pi k(\omega)}{\lambda} \tag{11}$$

Reflectivity provides a relationship that indicates the percentage of light reflected from the surface of material which is defined as,

$$R(\omega) = \left|\frac{\sqrt{\varepsilon(\omega)} - 1}{\sqrt{\varepsilon(\omega)} + 1}\right|^2 \tag{12}$$

The formula for the perovskite's conductivity is

$$\sigma(\omega) = \frac{2W_{c\nu}\hbar\omega}{\overrightarrow{E_0^2}} \tag{13}$$

where $W_{c\nu}$ stands for transition probability per unit time. Figure 7, respectively, display the various optical characteristics of $SbXO_3$ (X=Al and Ga) that were computed in this study. The 0 Hz limit $\varepsilon_1(0)$, which simply indicates the electronic factor of the dielectric function, is the most important part of the $\varepsilon_1(\omega)$ spectrum. For $SbAlO_3$ and SbGaO3, the observed static dielectric function values are 12.02 and 8.65, respectively. The two parts of the photon's dielectric function with an energy between 0 and 10 eV are displayed in Fig. 7a, b. Figure 7a illustrates how the electronic polarizability is derived from the $\varepsilon_1(\omega)$. Initially, the real part of dielectric function $\varepsilon_1(\omega)$ increases and reaches maximum value of 14.23 & 12.5 at 3.2 eV and 4.0 eV in case of SbGaO3 and SbAlO3 respectively. After that, its value gradually decreases and falls below 0 in the region between 5.2 and 8.5 eV. Indicating that it is metallic, the actual dielectric function $\varepsilon_1(\omega)$ is negative.

Table 3 Calculated Optical and transport properties by mBJ

	Material property	$SbAlO_3$	$SbGaO_3$	References
Optical properties	$\varepsilon_1(0)$	12.02	8.65	[4, 51, 52, 53]
	n(0)	2.48	2.60	
	R(0)	0.18	0.19	
Transport properties (300 K)	$\sigma/\tau(10^{18}\Omega^{-1}\ m^{-1}\ s^{-1})$	1.79	5.70	
	S(μ/VK)	242.28	266.07	
	κ_l(W/mK)	7.0	3.62	
	κ_e/τ (10^{15}W/mKs)	1.49	0.41	
	PF(10^{11}W/K^{2}ms)	1.05	4.03	
	ZT			

Figure 7b represents the photonic response of $\varepsilon_2(\omega)$. High absorption is observed for $SbGaO_3$ than $SbAlO_3$. Figure 7c, d and Fig. 7a–d displays the results of the calculations made for the refractive index, extinction coefficient, conductivity, absorption coefficient, reflectivity, energy loss function and Table 3 lists the values of these parameters. Similar to the imaginary dielectric function $\varepsilon_2(\omega)$ in Fig. 7c,

the graph of the extinction coefficient $k(\omega)$ (Fig. 7d) has a similar nature. The static value of refractive index are determined to be 2.48 and 2.60 at zero frequency for SbAlO3 and SbGaO3 respectively. A substance's greater refractive index is determined by its ability to slow down photons as a result of interaction with the material. There is a relationship between electron density and bonding and refractive index. Ionic bonding materials have a lower refractive index than covalent materials, which share more electrons and have a higher photon interaction.

The $SbXO_3$ (X=Al and Ga) exhibits the reflectivity depicted in Fig. 8c, wherein the reflectivity at zero frequency is 0.2 and 0.19 respectively, reaches its peak of 0.54 and 0.58 at 6.5 eV and 7.50 eV respectively, the real component's the dielectric function $\varepsilon_1(\omega)$ turns negative as illustrated in Fig. 8c. As illustrated in Fig. 8d, which shows the reduction of electron energy traveling in system form with its bands approaching the plasma resonance, the function $L(\omega)$ is also connected to energy loss. Comparably, Fig. 8a displays the conductivity $\sigma(\omega)$ owing to the photon, which reaches its highest value of 6325.12 Ω^{-1} cm^{-1} and 7767.27 at 3.8 eV and 5.2 eV, the same energy at which Fig. 8b displays the maximum coefficient of absorption [35, 46].

3.4 Thermoelectric properties

Direct thermal-to-electric energy conversion is possible with thermoelectric materials[42–44]. Since perovskite materials can convert thermal energy into electrical energy, they are valuable for thermoelectric applications [45, 46]. They also have a high absorption coefficient and enhanced thermal efficiency [47, 48]. Boltzmann transport theory, which is used in the BoltzTraP program, is used to calculate the thermoelectric characteristics of the compounds using a dense k mesh 46 × 46 × 46. The efficiency of conversion of thermoelectric devices, defined as the [49], is defined as follows:

$$ZT = S^2 \frac{\sigma T}{\kappa}$$

here S, σ, T, and κ is the thermal conductivity. $\kappa = \kappa_e + \kappa_l$. Figure 9a–f displays the computed thermoelectric characteristics of the cubic $SbXO_3$ (X=Al and Ga) perovskites. The relationship between each of these characteristics and temperature were examined. Seebeck coefficient S is an important parameter that illustrates the thermoelectric behaviour of material whose calculated values are plotted in Fig. 9a. Both compounds have positive S value for the entire temperature range, implying the availability of p-type charge carriers. The $SbGaO_3$ at low temperature has highest value of S while $SbAlO_3$ at higher temperatures. The positive 'S' values of SbAl/GaO_3 increase thermal to electrical energy conversion power.

Additionally, the power factor (PF) is calculated and plotted in Fig. 9b, that illustrates the highest values for $SbGaO_3$, and both compounds increases to rising temperature due to rise of S. The findings of Fig. 9c indicate that the examined perovskites exhibit an increase in electrical conductivity per relaxation time σ/τ with increasing temperature. It is noteworthy that $SbGaO_3$ have much greater σ/τ values compared to $SbAlO_3$ throughout the temperatures.

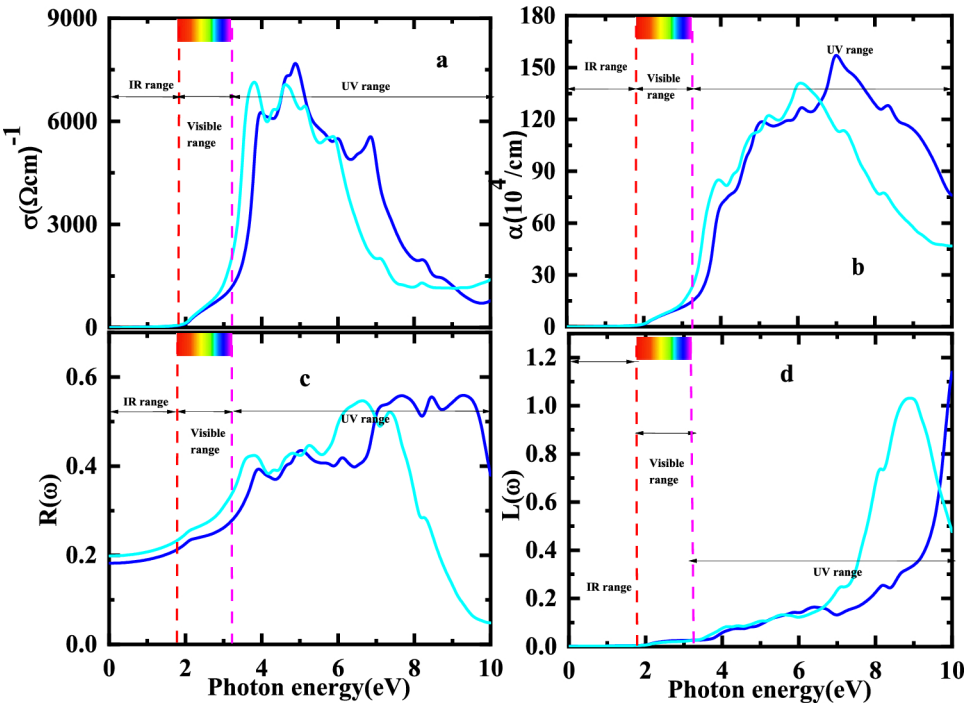

Fig. 8 **a** Optical conductivity σ(ω), (b) Absorption coefficient α(ω), **b** reflectivity R(ω), and **c** energy loss function L(ω) for $SbXO_3$ (X=Al, Ga)

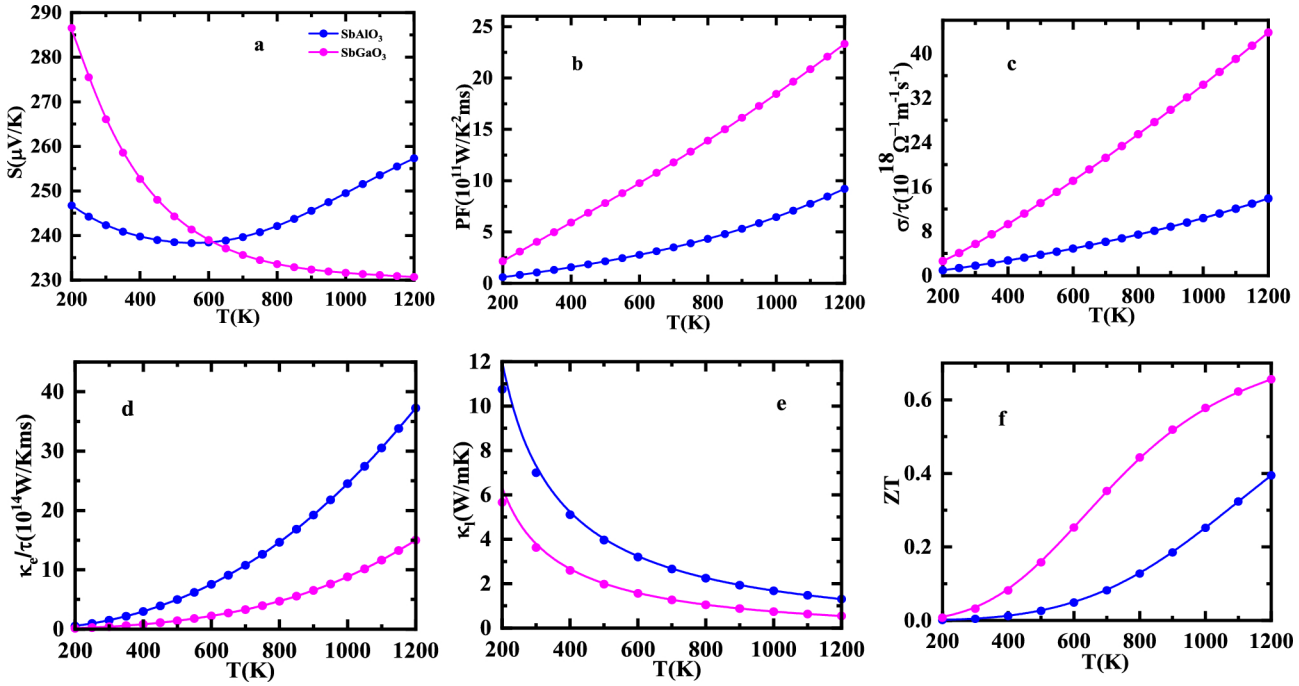

Fig. 9 Thermoelectric properties depending temperature: **a** Seebeck coefficient **b** Power factor **c** Electrical conductivity, **d** Thermal conductivity, **e** lattice thermal conductivity **f** Figure of merit for for $SbXO_3$ (X=Al, Ga)

The electronic contribution to the perovskites' thermal conductivity also increases, as shown in Fig. 9d. Up to 300 K, room temperature, both compounds show about equal thermal conductivity. Nevertheless, $SbAlO_3$ has a higher thermal conductivity than $SbGaO_3$ perovskites, with a significant increase above 300 K. Further isoelectronic compounds of the form $SbAlO_3$ and $SbGaO_3$ also showed an increase in electrical conductivity and thermal conductivity as a function of temperature. The styles of κ_e/τ are like σ/τ, but the ratio of κ_e/σ is of the order of 10^{-4} (Wiedemann Franz Law), that enhances the imperative of these systems for energy uses.

To take into consideration, the thermal conductivity (κ/τ), we independently estimated the electronic thermal conductivity (κ_e/τ) and lattice thermal conductivity (κ_l/τ) of systems under concern. Moreover, the BoltzTraP code is utilised to estimate κ_e/τ, and the Slack equation [50, 51] is applied to estimate lattice thermal conductivity κ_l during the calculation process:

$$\kappa_l = \frac{A\overline{M}\theta_D^3 V^{1/3}}{\gamma^2 T n^{2/3}}$$

where $\overline{M}$ is an average atomic mass, θ_D is Debye temperature, V is a volume per atom, n is a number of atoms per unit cell, γ is the Gruneisen parameter and A defines as:

$$A = \frac{2.43 \times 10^{-8}}{1 - \frac{0.514}{\gamma} + \frac{0.228}{\gamma^2}}$$

Hence, κ/τ is the combination of κ_e and κ_l as $\kappa = \kappa_t = \kappa_e + \kappa_l$. In Fig. 8 (e), we have drawn unique and merged modification of thermal conductivities with temperature for $SbAlO_3$ and $SbGaO_3$ perovskites, respectively. Figure 9e shows that $SbGaO_3$ has low κ_l as compared to the $SbAlO_3$ so it is best candidate for thermoelectric devices. The highest contribution of κ_e/τ to the total thermal conductivity for both materials are undoubtedly displayed in the figure in association to κ_l. The loss in κ_l is began by a rise in phonon scattering, that occurs as temperature progresses. It has been found that κ_e/τ significantly arises with temperature as well as marked an extreme at high temperature, which is the same tendency as of electrical conductivity. The computed quantities are sum up in Table 3 at room temperature.

The changes in Seebeck coefficients S and figure of merit ZT with respect to temperature are depicted in Fig. 9f. The performance of thermoelectric materials is evaluated using the transport parameter $ZT = \frac{S^2 T\sigma}{\kappa_e + \kappa_l}$, whereas the Seebeck coefficient calculates the potential difference between two distinct conductors or semiconductors when there is a temperature gradient between the two junctions. The fluctuations in band gap with temperature, as shown by equation, are the primary reason for increased ZT with temperature.

$$E_g(T) = E_g(0) - \frac{\alpha T^2}{(T+\beta)}$$

$E_g(T)$ and $E_g(0)$ represent the band gap energy at T and zero temperature, respectively, whereas α and β are constants. The relationship illustrates that growing the temperature reduces the band gap, which raises the figure of merit due to increased electrical mobility. These characteristics rise with rising temperature, as seen in both figures. There is a noticeable increase in the parameters between 200 and 300 K, and the parameters grow more gradually at higher temperatures. ZT has comparatively low values for $SbAlO_3$ than $SbGaO_3$ at throughout temperatures whereas $SbGaO_3$ has high figure of merit.

The transport properties of $SbXO_3$ are examined versus chemical potential $\mu - \varepsilon_F$ ranges from −2 to 4 eV for three different temperatures (300 K, 700 K, and 1200 K). Thermal transport coefficients such as $S, \sigma/\tau, \kappa/\tau, PF, ZT_e$ as a function of chemical potential at three fixed temperatures T=300 K, 700 K and 1200 K for $SbXO_3$ using mBJ-GGA are displayed in Fig. 9a–j. The peaks of S are found to be positive in the region of chemical potential indicating p-type behaviour of the studied compounds. The value of power factor PF, σ/τ & κ_e/τ are found to be high in the negative doping region indicating the possibility of n-type mode of the studied materials can have more applications in thermoelectric. Electrical conductivity is determined by the number of free carriers available for conduction, which distinguishes between n-type (electrons) and p-type (holes) semiconductors []. The Fermi level is at the valence band, indicating that free holes for conduction are more easily obtainable than electrons. The electrical conductivity in the chemical potential is depicted in Fig. 10g, h. The chemical potential $(\mu - \varepsilon_F)$ is the energy necessary to add or eliminate electrons by resolving Coulomb's repulsive and attractive forces. Electrical conductivity rises at -2.0 eV for the both oxides $SbXO_3$ (X=Al, Ga) reaches to the peak value 9.7×10^{20} $(\Omega\cdot m\cdot s)^{-1}$ and 7.4×10^{20} $(\Omega\cdot m\cdot s)^{-1}$ at -1.0 eV respectively, because of Coulomb repulsive and attractive forces provide different resistances to the movement of carrier. The carriers for the positive value of chemical potential (n-type region) are electrons, which enhance electrical conduction gradually as the chemical potential increases. Furthermore, the temperature impact on electrical conduction demonstrates a gradually increasing tendency in electrical conductivity, as electrons/holes get more flexible for transportation at higher temperatures. The slope of $SbGaO_3$ has a greater value than $SbAlO_3$ because Al metal provides more electrons per unit cell.

The heat flow due to temperature change (∇T) per unit length named as thermal conductivity and can be stated by Fourier's law as q=−k∇T, where q, ∇T and k are heat efflux, temperature gradient and coefficient of thermal conductivity. κ/τ is divided into two parts: κ_e and κ_p. In n- or p-type semiconductors, particles are accessible for conduction, which reduces the κ_p. As a result, we have enlarged the electronic component of κ/τ in the current study. Figure 9I, j shows the computed values of κ/τ vs chemical potential. κ/τ implements the same trend as κ_e, however its value is minor relative to electrical conductivity to minimize the thermal-to-electrical conductivity stated in the Wiedemann–Franz formula LT=κ/σ, with a value in order of 10^{-6}, making them necessary for thermoelectric devices [45]. The thermal conductivity at room temperature is low as compared to the 1200 K at– 2.0 eV for both $SbXO_3$ (X=Al, Ga) compounds. The maximum value attained for both $SbXO_3$ (X=Al, Ga) compounds are 22×10^{15}W/mKs and 17.98×10^{15}W/mKs respectively.

The change in temperature between different metallic contacts at J=0 can be analysed to the term $J = -\sigma\nabla V - \sigma S\nabla T$, where J,∇V and ∇T signify the current density, potential gradient and temperature gradient, correspondingly. In the optimal state, the $\nabla V = -S\nabla T$. The value varies from positive to negative in the n-type area and remains zero in the p-type region [46] due to mobile hole carriers for electrical conductivity, which is illustrated in Fig. 10a, b. The Seebeck coefficient decrease step by step as per increase of temperature till to 1200 K in both positive and side Seebeck coefficient. Moreover, the Seebeck coefficient is high for $SbGaO_3$ than $SbAlO_3$ as shown in Fig. 10a, b. Thermoelectric performance may be assessed using several scales, such as $PF = \sigma S2$, that offer an approximate value without factoring thermal conductivity, and figure of merit, that takes into account the thermal impact. Power factor for both compounds is higher at 1200 K but at 300 K power factor is minimum as compared to the other given temperature values. $SbGaO_3$ attain high power factor near the fermi level but $SbGaO_3$ has for away from the fermi level as shown in the Fig. 10c, d. The ZT Values attained approximately 1 with room temperature for both $SbXO_3$ (X=Al, Ga) materials as demonstrated in Fig. 10e, f. Our estimated outcomes are regarded and estimated up to some extent because they don't account for the phonon effect. Figure 9c, d depicts the observed PF, which has maximal values in two parts: $\mu - E_f(0)$ and 1 eV due to the combined effect of electrical conductivity as well as the S.

4 Conclusions

In conclusion, we examined the structural, electrical, optical, and thermoelectric characteristics of $SbXO_3$ (X=Al, Ga) based perovskites by employing FP-LAPW technique applied in the DFT built in Wien2k code. The studied

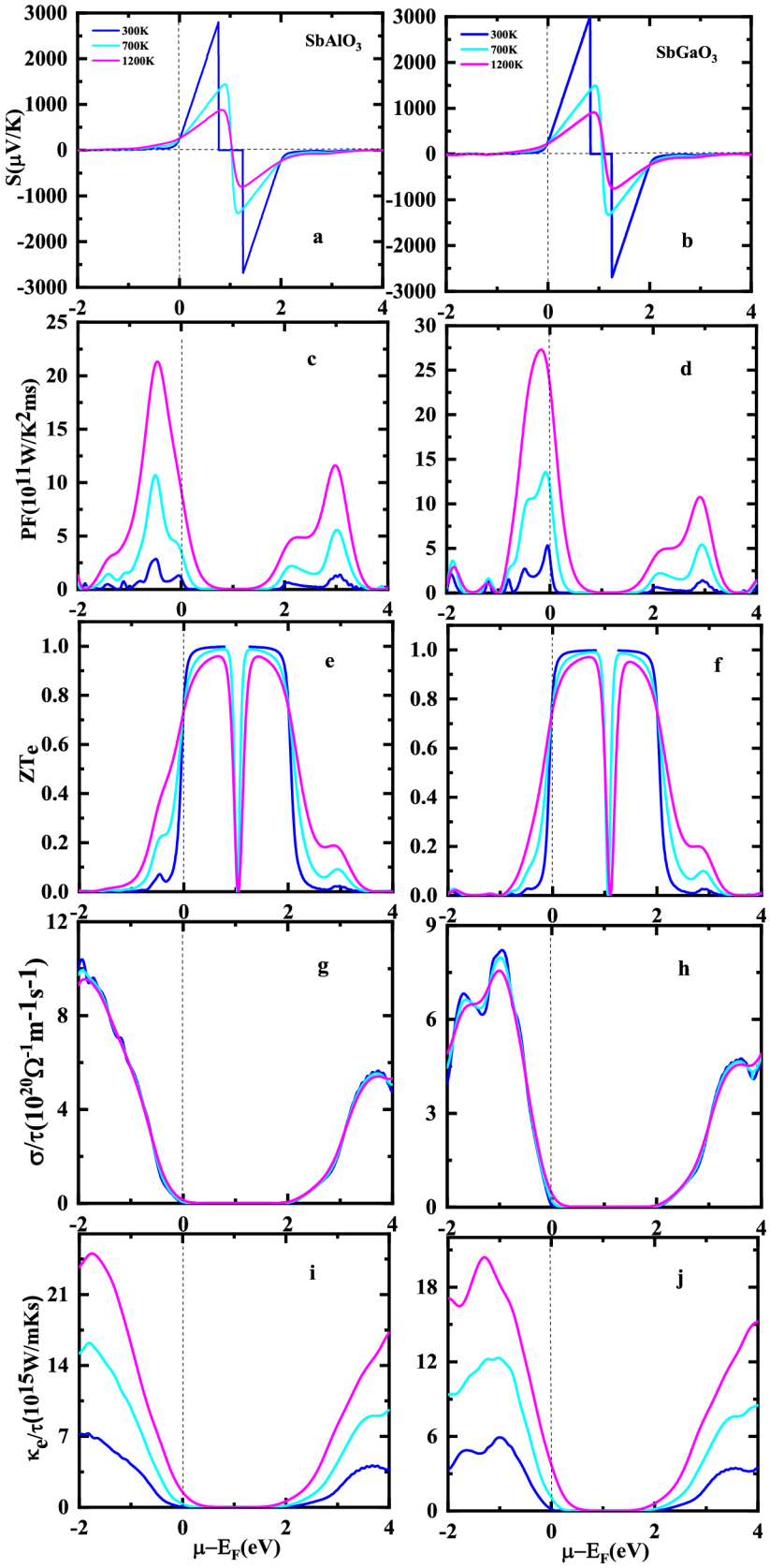

Fig. 10 Thermoelectric properties against chemical potential: **a**, **b** Seebeck coefficient **c**, d Power factor **e**, **f** Figure of merit, **g**, **h** Electrical conductivity, **i**, **j** Thermal conductivity for for $SbXO_3$ (X=Al, Ga)

perovskites are found to be structurally as well as thermodynamically stable as per the computed values of tolerance factor and formation & cohesive energy. The semiconductor behavior of $SbXO_3$ was confirmed by the presence of direct band gap, semiconductor for $SbAlO_3$ with $E_g = 2.074eV$ and for $SbGaO_3$ with $E_g = 2.059eV$. The band structure and DOS plots revealed that the band gap of the considered p-type semiconductors. $SbXO_3$ shows excellent absorption in the visible region indicating its application in optoelectronic devices. The static refractive index is 2.48 and 2.60 for mBJ-GGA Moreover, A significant conductivity and good figure of merit value are shown at room temperature. $SbGaO_3$ has a higher thermal efficiency than $SbAlO_3$ due to its narrower band gap and strong electrical conductivity.

Acknowledgements The authors extend their appreciation to King Saud University for funding this work through Researchers Supporting Project number (RSPD2025R993), King Saud University, Riyadh, Saudi Arabia.

Author Contributions All persons who meet authorship criteria are listed as authors, and all authors certify that they have participated sufficiently in the work to take public responsibility for the content, including participation in the concept, design, analysis, writing, or revision of the manuscript. Jaidev Kumbhakar, Arti Saxena, Anshuman Srivastava, Ramesh Sharma—Conceptualization, Methodology, Investigation, Formal Analysis, Software, Writing- Original draft preparation, Supervision. Jisha Annie Abraham, Mumtaz Manzoor, Ahmed Ahmed Ibrahim, Mohammed El-Meligy—Writing- Original draft preparation, Visualization, Investigation. Writing- Reviewing and Editing, funding acquisition.

Funding The authors present their appreciation to King Saud University for funding this research through Researchers Supporting Program number (RSPD2025R993), King Saud University, Riyadh, Saudi Arabia.

Data Availability No datasets were generated or analysed during the current study.

Declarations

Conflict of Interest The authors declare no competing interests.

References

1. M. Manzoor, D. Behera, R. Sharma, M.W. Iqbal, S.K. Mukherjee, R. Khenata, S.S. Alarfaji, H.A. Alzahrani, Investigation of the structural, mechanical, optoelectronic and thermoelectric characteristics of cubic GeTiO3: An ab initio study. Mater. Today Commun. **34**, 105053 (2023)
2. M. Manzoor, M.W. Iqbal, R. Sharma, J.A. Abraham, Exploration of structural, electronic, optical, mechanical, thermoelectric, and thermodynamic properties of XInO3 (X= As, Sb) compounds for energy harvesting applications. Int. J. Energy Res. **46**, 13409–13423 (2022)
3. S. Maqsood, A.U. Rahman, M. Nawaz, M.A. Ahmad, M. Manzoor, N. Noor, S.A. Abdelmohsen, Ab-initio method to investigate organic halide based double perovskites (CH3NH3) 2AgMBr 6 (M= Sb, Bi) for opto-electronic applications. J. Market. Res. **17**, 649–657 (2022)
4. A. Nazir, E.A. Khera, M. Manzoor, B.A. Al-Asbahi, Y.A. Kumar, R. Sharma, A density functional theory study of the structural, mechanical, optoelectronics and thermoelectric properties of InGeX3 (X= F, Cl) perovskites. Polyhedron **257**, 117009 (2024)
5. D. Oudrane, I. Bourachid, H. Bouafia, B. Djebour, B. Sahli, B. Abidri, D. Rached, Computational insights into the structural, mechanical, optical, electronic and magnetic properties of EuTiO3 semiconductor in cubic-perovskite using FP-LAPW method. Mater. Sci. Semicond. Process.Semicond. Process. **142**, 106455 (2022)
6. D. Oudrane, I. Bourachid, H. Bouafia, B. Sahli, B. Abidri, D. Rached, Computational insights in predicting structural, mechanical, electronic, magnetic and optical properties of EuAlO3 cubic-perovskite using FP-LAPW method. Comput. Condens. Matter. **26**, e00537 (2021)
7. N. Murali, K.E. Babu, P.S. Taddesse, A. Ramakrishna, D. Parajuli, R.P.N. Pramila, B. Suryanarayana, B.K. Babu, K. Samatha, V. Veeraiah, Theoretical investigation of structural, electronic, dielectric and optical characteristics of cubic perovskite BaCeO3. Process. Appl. Ceram. **15**, 351–356 (2021)
8. M. Acharya, S. Mack, A. Fernandez, J. Kim, H. Wang, K. Eriguchi, D. Meyers, V. Gopalan, J. Neaton, L.W. Martin, Searching for new ferroelectric materials using high-throughput databases: an experimental perspective on BiAlO3 and BiInO3. Chem. Mater. **32**, 7274–7283 (2020)
9. M. Asghar, M.W. Iqbal, M. Manzoor, N.A. Noor, M. Zanib, R. Sharma, H. Ullah, S. Aftab, T. Zahid, A computational insight of the lead-free double perovskites Rb2AgSbCl6 and Rb2AgSbBr 6 for optoelectronic and thermoelectric applications. Int. J. Energy Res. **46**, 24273–24285 (2022)
10. D. Behera, M. Manzoor, S.K. Mukherjee, Incorporation of Te in enhancing thermoelectric response of AeAg2SeTe (Ae= Sr, Ba) compounds: A DFT insight. Comput. Condens. Matter. **33**, e00757 (2022)
11. H. Wang, C. Zhang, W. Huang, X. Zou, Z. Chen, S. Sun, L. Zhang, J. Li, J. Cheng, S. Huang, Research progress of ABX 3-type lead-free perovskites for optoelectronic applications: materials and devices. Phys. Chem. Chem. Phys. **24**, 27585–27605 (2022)
12. S. Wang, M. Huang, Y.N. Wu, S. Chen, Absolute volume deformation potentials of inorganic ABX3 halide perovskites: the chemical trends. Adv. Theory Simul. **4**, 2100060 (2021)
13. Y. Wang, H. Zhang, J. Zhu, X. Lü, S. Li, R. Zou, Y. Zhao, Anti-perovskites with exceptional functionalities. Adv. Mater. **32**, 1905007 (2020)
14. M. Manzoor, N. Noor, M.W. Iqbal, M. Rashid, H. Ullah, A. Dahshan, DFT study of electronic, optical, and elastic properties of double perovskites Rb2YAgX6 (X= Br, I) compounds for optoelectronic device applications. Phys. Scr. **98**, 035703 (2023)
15. A. Nazir, A. Dixit, E.A. Khera, M. Manzoor, R. Sharma, A. Moayad, A DFT exploration of the optoelectronic and thermoelectric features of a novel halide double perovskite A 2 YAuI 6 (A= Rb, Cs) for solar cell and renewable energy applications. Mater. Adv. **5**, 4262–4275 (2024)
16. M.R. Walden, C.V. Ciobanu, G.L. Brennecka, Stability of epitaxial BiXO3 phases by density-functional theory, APL Mater. **8**,081106 (2020)
17. J. Kaczkowski, First-principles study of structural, electronic, ferroelectric, and vibrational properties of BiInO3 under high pressure. J. Phys. Chem. Solids **134**, 225–237 (2019)
18. L.-K. Gao, X.-S. Qi, Y.-L. Tang, First-principles study on the electronic structure, magnetic properties, elastic constants and sound velocity of the monoclinic crystal BiNiO3 under pressure. Results Phys. **58**, 107468 (2024)

19. X. Zhou, X. Peng, H. Xu, Y. Hao, H. Li, B.-P. Zhang, Bi compensation and poling process to enhance piezoelectric properties of BiFeO3-BaTiO3 lead-free piezoceramics. Ceram. Int. **50**, 35405–35413 (2024)
20. M. Zanib, M.W. Iqbal, M. Manzoor, M. Asghar, R. Sharma, N.N. Ahmad, S.M. Wabaidur, M.A. Habila, S.A. Abdelmohsen, A.M. Abdelbacki, A DFT investigation of mechanical, optical and thermoelectric properties of double perovskites K2AgAsX6 (X= Cl, Br) halides. Mater. Sci. Eng. B **295**, 116604 (2023)
21. M. Manzoor, M.W. Iqbal, M. Imran, N. Noor, A. Mahmood, Y.M. Alanazi, S. Aftab, Probing direct bandgap of double perovskites Rb2LiTlX6 (X= Cl, Br) and optoelectronic characteristics for Solar cell applications: DFT calculations. J. Market. Res. **18**, 4775–4785 (2022)
22. D. Parajuli, K. Ramanjaneyulu, N. Murali, A. Ramakrishna, K.M. Batoo, K. Samatha, V. Veeraiah, Structural, electronic, and optical properties of cubic perovskites BiMO3 (M= Al, Ga & In)–A computational study. Inorg. Chem. Commun.. Chem. Commun. **158**, 111466 (2023)
23. A. Acharya, *The end of American world order*, vol. 6 (Polity Press Cambridge, 2014)
24. D. Behera, M. Manzoor, R. Sharma, M.W. Iqbal, S.K. Mukherjee, First principles insight on structural, opto-electronic and transport properties of novel zintl-phase AMg2Bi2 (A= Sr, Ba). J. Solid State Chem. **320**, 123860 (2023)
25. A. Nazir, E.A. Khera, M. Manzoor, B.A. Al-Asbahi, R. Sharma, Tunable opto-electronic and thermoelectric response of alkali based half-Heusler semiconductors AMgN (A= Rb, Cs) for sustainable energy: A computational approach. Mater. Sci. Eng. B **303**, 117338 (2024)
26. A. Nazir, E.A. Khera, M. Manzoor, B. Ali-Asbah, R. Sharma, High Spin Polarization and half-metallic ferromagnetism in novel Half-Heusler FeCrX (X= S, Se and Te) alloys using first-principles calculations. Solid State Commun.Commun. **397**, 115803 (2024)
27. K.M. Hossain, M.K. Rubel, M.K. Hossain, G. Ishraque Toki, L. Marasamy, R. Haldhar et al., Hydrothermal synthesis, phase analysis, and magneto-electronic characterizations of lead-free ferroelectric BM2+ (Zn, Ca, Mg) T-BFO system. ACS Omega **9**(8), 9147–9160 (2024)
28. M.S. Uddin, M.K. Hossain, M.B. Uddin, G.F. Toki, M. Ouladsmane, M.H. Rubel et al., An in-depth investigation of the combined optoelectronic and photovoltaic properties of lead-free Cs2AgBiBr 6 double perovskite solar cells using DFT and SCAPS-1D frameworks. Adv. Electron. Mater. **10**(5), 2300751 (2024)
29. M.S. Uddin, S. Rana, M.K. Hossain, A. Kumar, P. Kanjariya, P.S. Bains et al., Performance improvement and optimization of $Cs_2TiI_2Br_4$ perovskite solar cells with diverse charge transport materials via numerical analysis. J. Phys. Chem. Solids **198**, 112486 (2024)
30. A. Gherriche, A. Bouhemadou, Y. Al-Douri, S. Bin-Omran, R. Khenata, M. Hadi, Ab initio exploration of the structural, elastic, electronic and optical properties of a new layered perovskite-type oxyfluoride: CsSrNb2O6F. Mater. Sci. Semicond. Process.Semicond. Process. **131**, 105890 (2021)
31. A. Bouhemadou, O. Boudrifa, N. Guechi, R. Khenata, Y. Al-Douri, Ş Uğur et al., Structural, elastic, electronic, chemical bonding and optical properties of Cu-based oxides ACuO (A= Li, Na, K and Rb): An ab initio study. Comput. Mater. Sci.. Mater. Sci. **81**, 561–574 (2014)
32. S. Al-Qaisi, M. Abu-Jafar, G. Gopir, R. Ahmed, S.B. Omran, R. Jaradat et al., Structural, elastic, mechanical and thermodynamic properties of Terbium oxide: First-principles investigations. Results Phys. **7**, 709–714 (2017)
33. R. Khenata, H. Baltache, M. Sahnoun, M. Driz, M. Rérat, B. Abbar, Full potential linearized augmented plane wave calculations of structural and electronic properties of GeC, SnC and GeSn. Phys. B **336**(3–4), 321–328 (2003)
34. P. Blaha, K. Schwarz, G. Madsen, D. Kuasnicke, J. Luitz, *Introduction to WIEN2K, An Augmented Plane Wane Plus Local Orbitals Program for Calculating Crystal Properties* (Vienna University of technology, Vienna, 2001), p.2001
35. P. Blaha, K. Schwarz, G.K. Madsen, D. Kvasnicka, J. Luitz, *wien2k*, An augmented plane wave+ local orbitals program for calculating crystal properties. **60**, (2001)
36. L. Hedin, B.I. Lundqvist, Explicit local exchange-correlation potentials. J. Phys. C Solid State Phys. **4**, 2064 (1971)
37. M. Mesbahi, F. Serdouk, M. Benkhedir, A DFT Study of the Electronic and Optical Properties of Kesterite Phase of Cu2ZnGeS4 Using GGA, TB-MBJ, and U Exchange Correlation Potentials. Acta Phys. Pol. A. **134**, 358–361 (2018)
38. S. Aftab, S. Yousuf, M.U. Khan, R. Khawar, A. Younus, M. Manzoor, M.W. Iqbal, M.Z. Iqbal, Carrier polarity modulation of molybdenum ditelluride (MoTe 2) for phototransistor and switching photodiode applications. Nanoscale **12**, 15687–15696 (2020)
39. K. Schwarz, P. Blaha, G.K.H. Madsen, Electronic structure calculations of solids using the WIEN2k package for material sciences, Comput. Phys. Commun. **147**, 71–76 (2002)
40. G.K. Madsen, D.J. Singh, BoltzTraP. A code for calculating band-structure dependent quantities. Comput. Phys. Commun.. Phys. Commun. **175**, 67–71 (2006)
41. T. Katsura, Y. Tange, A simple derivation of the Birch-Murnaghan equations of state (EOSs) and comparison with EOSs derived from other definitions of finite strain. Minerals. **9**, 745 (2019)
42. M. Ryan, J.-P. Fleurial, Where there is heat, there is a way: thermal to electric power conversion using thermoelectric microconverters. Electrochem. Soc. Interface. Soc. Interface. **11**, 30 (2002)
43. A. Feldhoff, Power conversion and its efficiency in thermoelectric materials. Entropy **22**, 803 (2020)
44. V. Jovanovic, S. Ghamaty, J.C. Bass, New thermoelectric materials and applications. In: 13th InterSociety Conference on Thermal and Thermomechanical Phenomena in Electronic Systems. 2012. IEEE.
45. A.-K. Trinh, I. González, L. Fournier, R. Pelletier, F.J. Lesage, Solar thermal energy conversion to electrical power. Appl. Therm. Eng. **70**, 675–686 (2014)
46. P.L. Hagelstein, Thermal to electric energy conversion, in *Condensed Matter Nuclear Science*. (World Scientific, 2006), pp.305–314
47. S. Zhu, G. Yu, Y. Ma, Y. Cheng, Y. Wang, S. Yu, Z. Wu, W. Dai, E. Luo, A free-piston Stirling generator integrated with a parabolic trough collector for thermal-to-electric conversion of solar energy. Appl. Energy **242**, 1248–1258 (2019)
48. E. Açıkkalp, L. Chen, M.H. Ahmadi, Comparative performance analyses of molten carbonate fuel cell-alkali metal thermal to electric converter and molten carbonate fuel cell-thermo-electric generator hybrid systems. Energy Rep. **6**, 10–16 (2020)
49. M.W. Iqbal, M. Manzoor, N. Noor, I. Rehman, N. Mushahid, S. Aftab, Y.M. Alanazi, H. Ullah, A.M. Afzal, Tuning of the electronic bandgap of lead-free double perovskites K2AgBiX6 (X= Cl, Br) for solar cells applications and their thermoelectric characteristics. Sol. Energy **239**, 234–241 (2022)
50. E.A. Khera, A. Nazir, M. Manzoor, M. Ayub, F. Hussain, B.A. Al-Asbahi et al., First principles exploration of structural stability, optoelectronic and thermoelectric properties of BaXO3 (X= Hf, Ti, V) for solar cell applications. Mater. Today Commun. **39**, 108629 (2024)
51. K. A. Alrashidi, A. Dixit, A. Nazir, E. A. Khera, S. Mohammad, M. Manzoor, et al. A DFT Approach to Insight on the structural, optoelectronic and thermoelectric properties of cubic perovskites

YXO3 (X= Ga, In) for renewable energy applications. J. Inorg. Organometall. Polym. Mater. 1–15 (2024). https://doi.org/10.1007/s10904-024-03362-3
52. E.A. Khera, A. Nazir, Z. Ahmed, M. Manzoor, H. Ullah, S. Ansar et al., Computational prediction of structural, optoelectronic, thermodynamic, and thermoelectric response of the cubic perovskite RbTmCl3 via DFT-mBJ+ SOC Studies. Phys. Status Solidi (b). **262**, 2400123 (2024)
53. Y. Wei, X. Sun, X. Meng, Z. Li, L. Zhang, K. Zhou, Z. Ma, Enhancing the properties of Cd-free MgZnS buffer for solar cells by co-sputtering ZnS and Mg targets. Mater. Today Commun. **39**, 108766 (2024)
54. C. Gao, J. Zhu, S. Ye, M. Li, H. Wang, J. He, Novel high-entropy perovskite titanate: A potential thermal protective material with improved thermophysical properties. J. Eur. Ceram. Soc. **45**(2), 116878 (2025)